Strategies to improve photocatalytic activity of nanoscale zero valent iron decorated MoS_2

Wu, Xi; Wang, Xiangyu; Lynch, Iseult; Guo, Zhiling; Zhang, Peng; Wu, Lisi; Deng, Youxue; Xie, Yu; Ning, Ping; Ren, Nanqi

DOI:
10.1016/j.jclepro.2023.135865

Document Version
Peer reviewed version

Citation for published version (Harvard):
Wu, X, Wang, X, Lynch, I, Guo, Z, Zhang, P, Wu, L, Deng, Y, Xie, Y, Ning, P & Ren, N 2023, 'Strategies to improve photocatalytic activity of nanoscale zero valent iron decorated MoS_2: Construction of novel S-scheme nanoflower heterojunction with advanced visible-light degradation of tetracycline', *Journal of Cleaner Production*, vol. 388, 135865. https://doi.org/10.1016/j.jclepro.2023.135865

Strategies to improve photocatalytic activity of nanoscale zero valent iron decorated MoS_2: Construction of novel S-scheme nanoflower heterojunction with advanced visible-light degradation of tetracycline

Xi Wu[a], Xiangyu Wang[a,b,*], Iseult Lynch[b], Zhiling Guo[b], Peng Zhang[b], Lisi Wu[b], Youxue Deng[a], Yu Xie[a], Ping Ning[a,*], Nanqi Ren[c]

[a] *Faculty of Environmental Science and Engineering, Kunming University of Science and Technology, Kunming 650500, China*

[b] *School of Geography, Earth and Environmental Sciences, University of Birmingham, Birmingham, B15 2TT, UK*

[c] *School of Municipal and Environmental Engineering, Harbin Institute of Technology, Harbin 150090, China*

*** Corresponding Authors**

E-mail addresses: imusthlee2014@sina.com (X. Wang), ningping58-2015@sina.com (P. Ning).

Word count: 8335

Abstract

Although both MoS_2 and nanoscale zero valent iron have presented bright prospects for environmental remediation. The constrained conductivity of MoS_2 and the passivation and aggregation of Fe^0 still retained challenges. Given this, innovative strategies of activating the passivation layers of Fe^0 into semiconductors by photocatalysis and constructing S-scheme nanoflower heterojunctions with MoS_2 (Fe^0@MoS_2) were fabricated. The results revealed that Fe^0@MoS_2 exhibited enhanced efficiency toward visible-light degradation of tetracycline, which was 3.20 and 1.27 times as high as that of bare MoS_2 and Fe^0, respectively. The boosted activity

was attributed to the cooperation of MoS_2 and Fe^0. The synergistic effects stemmed from the following mechanisms: (1) the fluffy nanoflower-like structure and widened interlayer spacing of MoS_2 facilitated the dispersion of Fe^0, guaranteeing its enhanced adsorption and reduction capacity; (2) the conductivity of MoS_2 was remarkably improved due to the doping of the passivation layers of Fe^0, and the layers were activated as semiconductors by visible-light, causing the establishment of S-scheme heterojunctions between them and MoS_2. Moreover, the kinetics, stability, recyclability, and optical characteristics of Fe^0@MoS_2 were confirmed comprehensively. The potential routes for TC elimination deriving from the action of $\bullet O_2^-$ and h^+ were proposed. These findings provided novel strategies for construction of Fe^0-based S-scheme heterojunction with advanced visible-light-induced degradation performance.

Keywords: MoS_2 nanoflower; Nanoscale zero valent iron; Synergistic effect; S-scheme heterojunction; Tetracycline photodegradation

1. Introduction

Over the years, antibiotics have been extensively employed for the cure of illnesses of living organisms (Chen et al., 2022). Among them, increasing attention has been devoted to tetracycline (TC) with broad spectrum and good efficacy (Zhou et al., 2022). However, numerous studies have shown that TC cannot be accepted fully by organisms, leading to non-negligible amounts of TC being discharged into the ecosystem (Zhu et al., 2019). The bio-refractory TC eventually presents grave risks to organism wellness and ecosystem stability because of the emergence of resistance genes (Zhou et al., 2020; Zhou et al., 2022). Thus, it is urgent to efficiently degrade TC in water body.

Photocatalyst, such as TiO_2, is commonly recognized as an ideal material to degrade TC due to its environmental friendliness (Liu et al., 2022a; Liu et al., 2022b; Liu et al., 2022c; Lu et al., 2018).

However, the drawback that only absorbs UV light limits the large-scale application (Chen et al., 2015; Chen et al., 2020; Hu et al., 2022; Hu et al., 2023). Conversely, the narrow band gap of MoS_2 makes it easy to be excited by visible-light, and the 2D layered structure ensures more permeable channels (Ahmaruzzaman and Gadore, 2021; Wu et al., 2018). So far, MoS_2 has been considered with application prospects in those fields such as energy storage, electronic devices and environmental remediation (Li et al., 2020; Liu et al., 2022a; Lu et al., 2018; Zhang et al., 2016).

Although molybdenum disulfide (MoS_2) has also received extensive attention as a classic transition-metal dichalcogenides layered photocatalyst (Zhang et al., 2016; Zheng et al., 2016), the speedy compounding of photo-excited carriers and constrained conductivity of bare MoS_2 inevitably limit its photocatalytic performance (Li et al., 2021; Wang et al., 2018). To address these drawbacks, Jiang et al. constructed a Z-scheme $MoS_2/CaTiO_3$ heterostructure and achieved enhanced photodegradation for TC (Jiang et al., 2020). Li et al. synthesized a recyclable like-Z-scheme heterojunction of $MoS_2@Fe_3O_4@Cu_2O$, and such a structure ensured efficient photodegradation of TC (Li et al., 2021). Thus, assembling heterojunction composites with other semiconductors can act as an attractive tactic to strengthen the photocatalytic potential of MoS_2.

Meanwhile, nanoscale zero valent iron (nZVI, Fe^0) is attracting growing attention towards antibiotics elimination on account of its cost-effectiveness, considerable reduction capacity and environmental friendliness (Cao et al., 2021; Qiao et al., 2018; Weng et al., 2021). However, the inherent magnetism of Fe^0 causes its strong tendency to aggregate, thereby inhibiting its adsorption and reactivity to pollutants (Hu and Li, 2018; Shao et al., 2020). Another crucial element restricting the development of Fe^0 is the creation of an oxide film on the shell during the degradation reaction (Tian et al., 2021). Currently, the general opinion is that the dense oxide layer is mainly composed of iron oxide (Fe_2O_3), which is harmful to the reactivity and lifetime of Fe^0 (Li et al., 2021; Tian et

al., 2021; Xu et al., 2019). However, the cutting-edge researches demonstrate that Fe_2O_3 has notable potential for photocatalysis due to its environmental benign and visible-light absorption (Wang et al., 2021; Zhao et al., 2021; Zhang et al., 2021). Inspired by these, the passivation layer of Fe^0 may be excited by visible-light, and since Fe_2O_3 and MoS_2 have a matching energy band structure, a heterojunction can be constructed between them to boost the conductivity of MoS_2. Meanwhile, the typical layered structure of MoS_2 is expected to effectively improve the dispersion of nZVI particles, thereby strengthening their reactivity.

Based on the aforementioned considerations, we innovatively proposed the strategy of constructing visible-light-driven S-scheme heterojunction between Fe^0 and MoS_2 nanoflower as photocatalyst that was expected to exhibit superior photodegradation performance and synergistic effects. The heterojunction was beneficial to the enhancement of the dispersion, adsorption, reduction capacity of Fe^0. Moreover, for the first time, our research fabricated Fe^0@MoS_2 composite via an easy-to-implement method for visible-light photodegradation of antibiotic to investigate the feasibility and synergistic effects of converting the oxide coating of nZVI to a semiconductor. The systematic assessments and multiple characterization were adopted to confirm the successful constructing of an efficient heterojunction between the passivation layer of Fe^0 and MoS_2 nanoflower. To the best of our knowledge, Fe^0@MoS_2 as a S-type heterojunction photocatalyst to achieve efficient synergistic visible-light photo-elimination of TC has not been reported yet. In the meantime, the oxide layer on the surface of Fe^0 enhanced the segregation and transport of photo-excited charges in MoS_2 nanoflower, and it was activated to a semiconductor by visible-light radiation, which was capable of building a high-performance heterojunction after combining with MoS_2. Besides, we also provided an innovative attempt of constructing a heterojunction among the oxide coating of Fe^0 with MoS_2 nanoflower in light of effectively using

the high semiconductivity of the passivation layer to achieve enhanced photocatalytic performance.

Furthermore, the ultrahigh loading of Fe^0 in the composite and the generation of a passivation layer were observed. The excellent TC photodegradation performance, stability and kinetics of Fe^0@MoS_2 were recorded. Additionally, the visible-light utilization potential as well as energy band architecture of the passivation layer and MoS_2, and in-situ assembly of the S-type nanoflower heterojunction among the two were investigated deeply. The mechanism and reaction paths of TC photocatalytic based on the excited and reactive species were systematically elucidated.

2. Materials and methods

2.1. Materials

The diverse materials involved in all experiments were described in the Supplementary Material.

2.2. Synthesis of heterojunction

2.2.1. MoS_2 nanoflowers

MoS_2 nanoflowers were assembled from numerous nanosheets manufactured via a simple hydrothermal process. For formation of homogeneous solution, 2.8425 g of $H_{32}Mo_7N_6O_{28}$ and 5.2523 g of CH_4N_2S were sequentially dissolved into 80 mL ultrapure water (UPW), and magnetically stirred for 30 min. Afterwards, the solution was loaded into a 100 mL Teflon-lined autoclave and placed at 180 °C for 24 h. After cooling overnight, the prepared MoS_2 nanoflowers were rinsed and filtered up to 3 cycles with UPW, then vacuum dried and preserved for further use.

2.2.2. Fe^0@MoS_2

Fe^0@MoS_2 was fabricated using a liquid deposition approach in one anaerobic box (Fig. 1). In detail, fixed doses of $FeSO_4·7H_2O$ and MoS_2 nanoflowers were separately dissolved in UPW under continuous stirring. After that, overdosed KBH_4 was gradually injected to this mixture. After

titration, the obtained products were stirred for an extra 30 min, and then washed and filtered with UPW, ethanol and acetone respectively. Eventually, the synthesized Fe^0@MoS_2 were desiccated and saved in one anoxic dryer. To explore the optimal performance of the heterojunction, Fe^0@MoS_2 with mass ratios of $FeSO_4 \cdot 7H_2O$ and MoS_2 of 1:2, 1:1, 2:1 were prepared and were named as Fe@MS-1, Fe@MS-2, Fe@MS-3 individually. For comparison, nZVI was synthesized via this liquid deposition approach lacking the doping of MoS_2 nanoflowers, and Fe@MS after half an hour of lightless reaction and after the photocatalytic reaction were designated as Fe_2O_3@MS, Reacted-Fe@MS respectively.

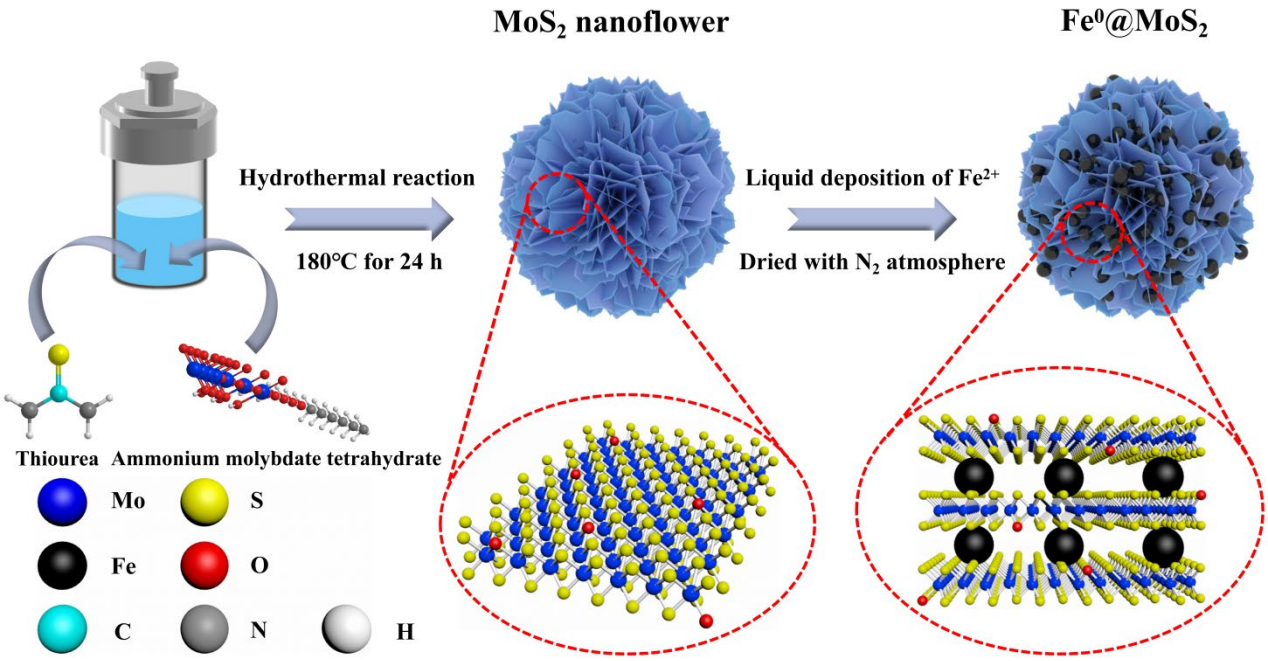

Fig. 1. Schematic diagram for the constructing procedure involving Fe^0@MoS_2 heterojunction.

2.3. Photodegradation test

The photodegradation activity of tetracycline using Fe^0@MoS_2 was assessed via a photochemical reaction device equipped with a 300 W xenon lamp (420 nm cut-off filter, ZQ-GHX-V, China). 10 mg of Fe^0@MoS_2 powder was spread in tetracycline solution (30 $mg \cdot L^{-1}$, 60 mL, pH = 6.5) and continuously stirred for 30 min in the absence of light (the model concentration of the TC solution (Table S1) was chosen based on the TC concentrations reported in

previous literature) (Hou et al., 2016). As the adsorption–desorption balance was achieved, the photoreaction was conducted with visible-light illumination. After 1 mL of samples were obtained, filtrated and diluted 10 folds, a UV–vis spectrophotometer (UV-1800PC, China) was adopted to quantify the residual TC levels in them at a wavelength of 357 nm. The following formula (1) was listed to calculate the degradation efficiency of TC (DE, %):

$$\mathrm{DE}\ (\%) = [(C_0 - C_t) / C_0] \times 100\% \quad (1)$$

where C_0 represents the initial content of TC, and C_t means the content of TC at time t (min). Moreover, cycling experiments with a total of 5 cycles were undertaken in order to investigate the photodegradation stability of Fe^0@MoS_2. The effects of light, catalyst dose, pH and TC concentration on the degradation efficiency of Fe^0@MoS_2 were also explored.

2.4. Characterizations

Characterization items and associated parameters for the multiple properties of nanomaterials were illustrated in the Supplementary Material.

3. Results and discussion

3.1. Morphology and structure of nanomaterials

The micro-morphology and architecture of nanomaterials initially reflects their ability to degrade pollutants. Accordingly, Fe@MS-2 is selected as a representative composite based on its optimal photocatalytic capacity for TC (shown in Section 3.2) and its morphology is observed and analyzed using scanning electron microscopy (SEM), transmission electron microscopy (TEM) and mapping techniques. As observed in Fig. 2a, the nZVI particles have a chain-like structure due to their inherent magnetic properties (Zhou et al., 2022). Interestingly, the as-prepared MoS_2 is in the form of nanoflowers (Fig. 2b–c), which consist of a large number of ultrathin nanosheets. After Fe^0 particles are deposited on MoS_2 nanoflowers (Fig. 2d–f), they are either distributed on the petals of

nanoflowers or confined between the petals. Apparently, Fe^0 particles exhibit a highly dispersed state in Fe@MS-2 by overcoming their inherent magnetism, and the number of their available active sites is further increased. Meanwhile, the fluffy nanoflower-like structure of the composite provides abundant channels, which facilitate the efficient transfer and adsorption of pollutants. As shown in Fig. 2g, the (110) plane of Fe^0 and the (100) plane of MoS_2 are observed by high-resolution TEM, indicating that Fe@MS-2 are successfully synthesized. From the test results of mapping (Fig. 2h), it can be seen that the composite contains O element in addition to Fe, Mo and S elements, reflecting the surface oxidation of nZVI or the doping of O during the hydrothermal synthesis of MoS_2. Furthermore, the high dispersion of nZVI and the successful preparation of composites are reconfirmed by mapping.

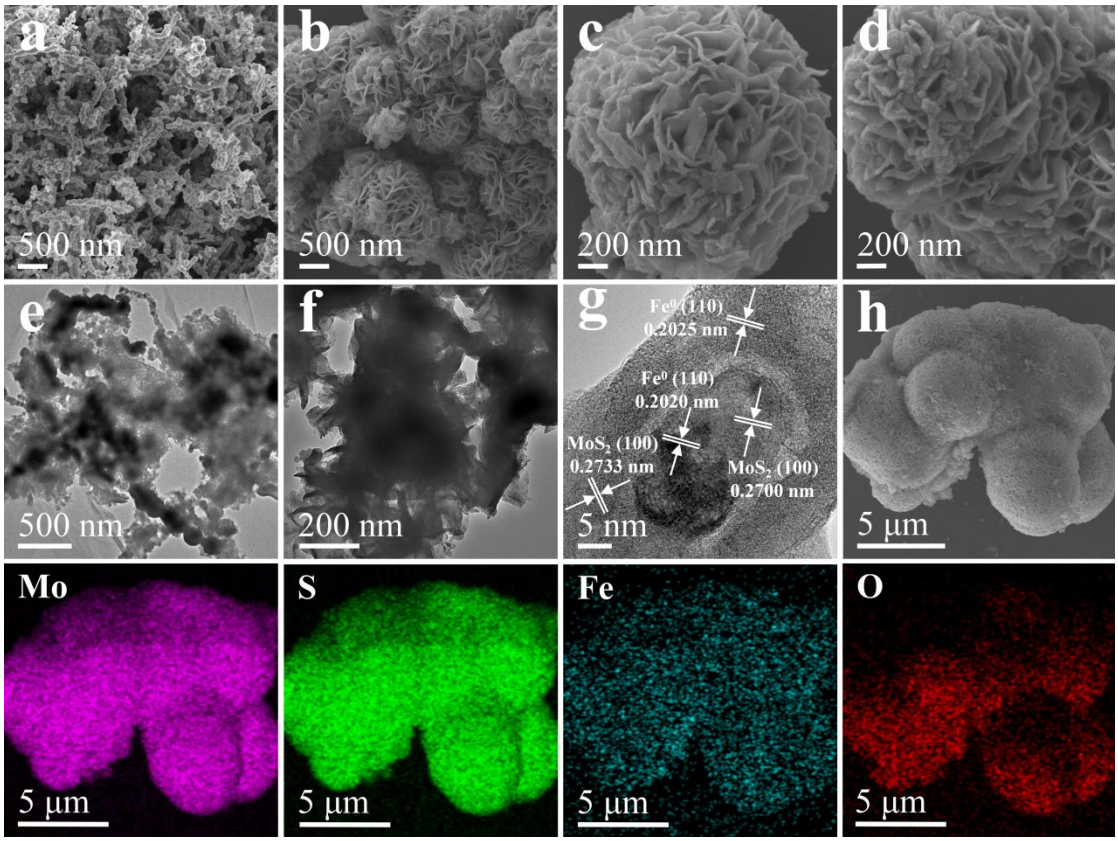

Fig. 2. SEM of (a) Fe^0, (b–c) MoS_2 nanoflowers. (d) SEM, (e–g) TEM and (h) mapping of Fe@MS-2.

The micro-structure of Fe@MS-2 is further characterized by X-ray diffraction (XRD) to explicate its more excellent photodegradation performance relative to bare MoS_2. As shown in Fig. 3a, the as-prepared Fe^0 has observable diffraction peaks at 2θ = 44.7° and 81.8°, which correspond to the (110) and (211) crystal facets of JCPDS No. 06-0696, respectively (Li et al., 2019). The significant diffraction peaks at 2θ = 13.8°, 32.5°, 35.5° and 57.6° are assigned to the (002), (100), (102) and (110) crystal facets of 2H-MoS_2 (JCPDS No. 37-1492) separately (Zheng et al., 2016). Among them, at low-angle region, the interlayer spacing of 2H-MoS_2 relative to the (002) crystal facet is 0.6155 nm (Bai et al., 2019). However, two new diffraction peaks appear at 2θ = 9.0° and 16.7° with the combination of Fe^0 and MoS_2. Such a diploid relationship illustrates the generation of a new layered construction with one broadened interlayer spacing of 0.95 nm relative to that of 0.6155 nm in 2H-MoS_2 (Ai et al., 2016; Bai et al., 2019). In Fe@MS-2, the characteristic diffraction peak of Fe^0 located at 2θ = 44.7° is detected, indicating the successful synthesis of the composite, which is consistent with the conclusions of TEM and mapping. Structural changes of Fe@MS-2 after dark reaction in TC solution for 30 min are observed. It is noteworthy that after the dark reaction of Fe@MS-2, new diffraction peaks located at 2θ = 17.6°, 24.2°, 29.1°, 35.3°, 39.1° and 50.0° appear with the almost disappearance of Fe^0 phase. These peaks correspond to the (113), (203), (206), (119), (209) and (2112) crystal facets of Fe_2O_3 (JCPDS No.25-1402), respectively. The phenomenon fully proves the surface of Fe^0 is oxidized to Fe_2O_3 after a lightless reaction for half an hour. The conclusion that the interlayer spacing of MoS_2 is widened is also confirmed by the high-resolution TEM. As can be seen from the TEM image of Fe@MS-2 (Fig. 3b), in addition to the (110) crystal facet of Fe^0 and the (100) crystal facet of MoS_2 being labeled, the (002) crystal facet of MoS_2 with a layer spacing of approximately 0.95 nm is also clearly observed. From the above results, it is clear that the doping of Fe^0 expands the interlayer spacing of MoS_2 from 0.6155 nm to

0.95 nm (Fig. 3c–d). This result may be responsible for the synthesis method of Fe@MS-2. Before the preparation, Fe^{2+} is fully dissolved and adsorbed onto MoS_2, subsequently, the Fe^{2+} adsorbed between the MoS_2 layers is reduced by KBH_4 to produce Fe^0, thus realizing the expansion of its interlayer spacing. Obviously, such an enlarged interlayer spacing facilitates the expose of available reactive centers and the diffusion and adsorption of contaminants.

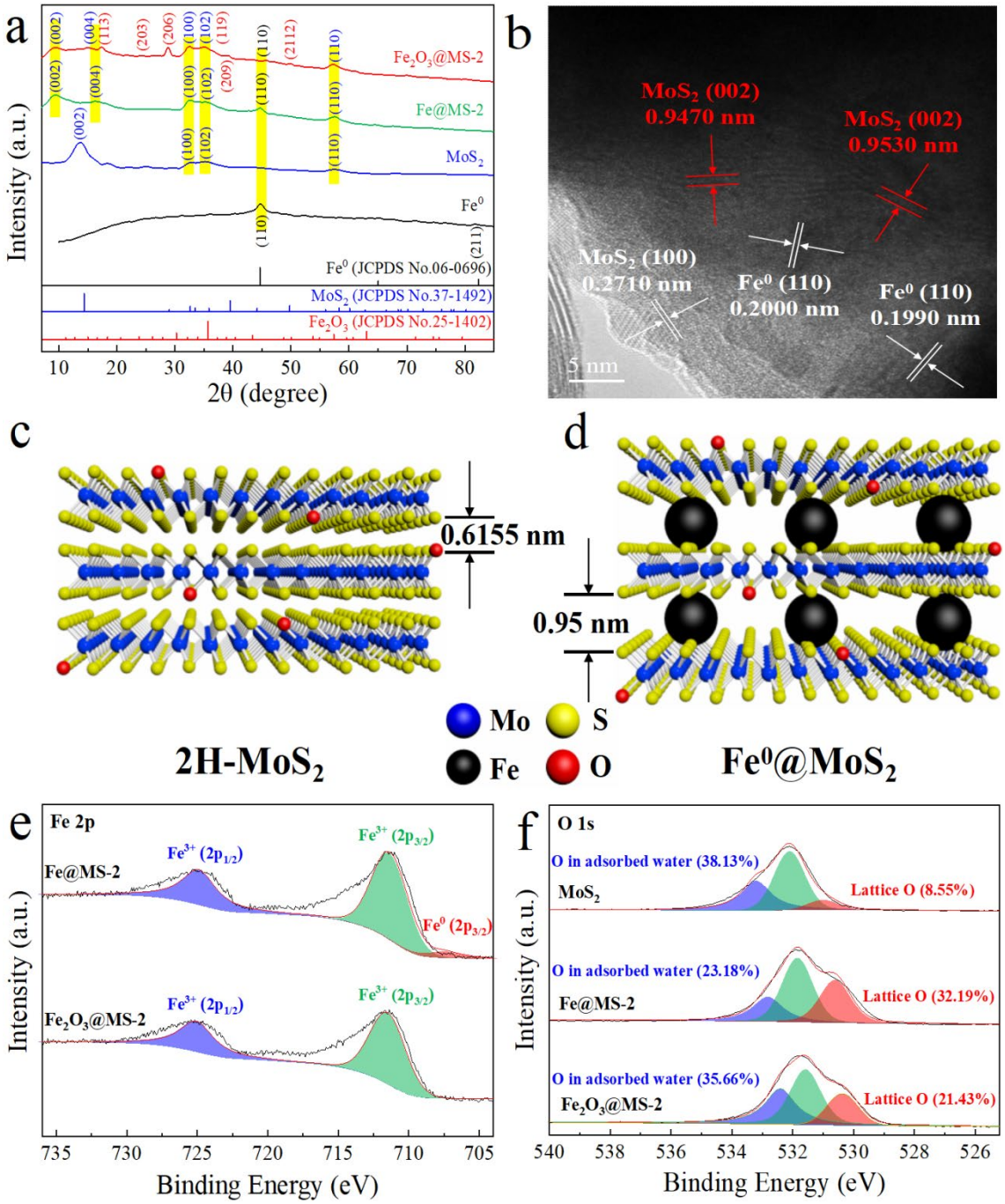

Fig. 3. (a) XRD results for nanomaterials. (b) High-resolution TEM image of Fe@MS-2. Schematic diagram of the comparison of interlayer spacing (c) before and (d) after MoS_2 loading with Fe^0. (e) Fe 2p and (f) O 1s XPS spectra of nanomaterials.

X-ray photoelectron spectroscopy (XPS) of nanomaterials are measured to gain insight into their structural changes during preparation and degradation. As depicted in Fig. S1a, XPS survey spectra indicate the existence of Fe, Mo, S, and O elements in Fe@MS-2, again demonstrating the successful preparation of composite. Mo 3d XPS spectra indicate the existence of Mo^{4+} and Mo^{6+} in Fe@MS-2 (Fig. S1b), and the generation of Mo^{6+} may originate from the slight oxidation of surface Mo^{4+} during the synthesis of composite (Sun et al., 2018; Zhang et al., 2020). The Fe $2p_{3/2}$ peak at 707.46 eV is assigned to Fe^0, and the Fe 2p peaks at 711.34 eV ($2p_{3/2}$) and 724.88 eV ($2p_{1/2}$) are ascribed to Fe_2O_3, which confirms the previously reported conclusion that the surface of nZVI has a slim oxide film (Fig. 3e) (Fang et al., 2010; Ling and Zhang, 2015). Nevertheless, the feature peak of nZVI vanishes after the lightless reaction for half an hour, and the peaks of Fe_2O_3 at 711.48 eV and 725.06 eV stay present. This phenomenon adequately demonstrates that the oxide coating on the nZVI becomes significantly thicker after dark reaction relative to that before the reaction, which is consistent with the results in XRD. Moreover, as shown in Fig. S2, the two characteristic peaks assigned to Fe_2O_3 are still existing after the photodegradation reaction of Fe@MS-2 (Reacted-Fe@MS-2), indicating that no new iron oxides are observed with prolongation of the reaction time. For O 1s XPS spectra (Fig. 3f), the O in adsorbed water of 3 samples (MoS_2, Fe@MS-2, Fe_2O_3@MS-2) shows a characteristic of first decreasing and then increasing, which originates from the drying process during the synthesis of Fe@MS-2 (Zhao et al., 2020). Subsequently, the composite reacts in TC solution resulting in the increment of O in adsorbed water. The peaks of 3 samples at about 530.60 eV correspond to lattice oxygen ($O_{lattice}$) (Zhao et al., 2020).

Pristine MoS_2 contains 8.55% of $O_{lattice}$, indicating the successful incorporation of oxygen rather than surface oxidation during the hydrothermal process, which again supports the conclusion in mapping (Xie et al., 2013). The $O_{lattice}$ content is significantly increased to 32.19% after the synthesis of Fe@MS-2, which may be due to the expanded interlayer spacing that facilitates more oxygen into the lattice of MoS_2. After 30 min of dark reaction, the $O_{lattice}$ content decreases from 32.19% to 21.43%, indirectly revealing the contribution of $O_{lattice}$ to TC degradation. Coupled with the XRD and XPS results, it is important that the dense passivation layer (Fe_2O_3) of Fe^0 is produced after 30 min of dark reaction, which establishes the basis for the building of heterojunctions among the passivation layer with MoS_2.

3.2. Photodegradation ability of nanomaterials

The photodegradation activity of nanomaterials for TC is assessed via a series of photocatalytic tests. It can be seen from Fig. 4a that tetracycline is highly stable without catalysts, even when exposed to visible-light. Conversely, there is an observable degradation of TC in the presence of catalysts. Among them, the photodegradation capacity of composites (Fe@MS-1, Fe@MS-2, Fe@MS-3) is generally stronger than that of single materials (Fe^0, MoS_2). Obviously, Fe@MS-2 achieves 97.37% of TC photodegradation efficiency after visible-light radiation for 45 min, which is 3.20 and 1.27 folds compared to that of bare MoS_2 and Fe^0 separately, showing superior TC removal ability. The better TC degradation performance of Fe^0@MoS_2 compared to single components is ascribed to the cooperative action among Fe^0 with MoS_2. The synergistic effect is manifested in two aspects, (1) the dispersion and anchoring of Fe^0 induced by MoS_2 facilitate the exposure of its more available active sites (confirmed in Section 3.1), showing enhanced adsorption and reduction ability; (2) doping of Fe^0 dramatically enhances the conductivity of MoS_2 (confirmed in Section 3.3), and MoS_2 and the dense oxide layer generated after the dark

reaction of Fe^0 form a heterojunction with excellent photocatalytic activity (confirmed in Section 3.4). In addition, undesirable TC degradation ability is observed in Fe@MS-1 and Fe@MS-3 compared with in Fe@MS-2, which stems from particles aggregation caused by excessive Fe^0, thus decreasing the exposure of available reactive centers. Contrarily, insufficient amount of nZVI is difficult to provide efficient reduction and photodegradation performance for TC. Surprisingly, Fe^0@MoS_2 exhibits a competitive TC degradation ability compared with catalysts in other related literatures (comparison of photodegradation performance of catalysts is marked in Table 1), indicating its potential application for tetracycline wastewater treatment.

The effects of light, catalyst dose, pH and TC concentration on the degradation performance of Fe@MS-2 are also explored. As depicted in Fig. S3a, a restricted TC degradation is achieved in the dark, however, a in-depth degradation of TC is triggered due to the illumination of visible-light. The reason for these phenomena lies in the formation of a dense passivation coating of nZVI after 30 min of dark reaction, which dramatically limits the reactivity of the catalyst by preventing the contact of Fe^0 with the contaminant in the absence of any driving force. After visible-light radiation, the optical potential of the passivation layer is excited (as confirmed in Fig. 5), and the layer constructs an S-scheme nanoflower heterojunction with MoS_2, leading to the in-depth photodegradation of TC. For the catalyst dose (Fig. S3b), the results indicate that the photodegradation efficiency of TC gradually improves with the increase of catalyst dose. However, the removal efficiency of TC is slightly diminished at a dose of 12 mg, which is due to the excessive dose instead affecting the visible-light absorption of the material. As presented in Fig. S3c, the findings reveal that Fe@MS-2 exhibits higher degradation efficiencies in acidic to neutral environments relative to that in alkaline environments. These stem from the fact that the acidic environment favors the dissolution of the oxide coating and the exposure of nZVI, and the alkaline

environment may lead to the formation of hydroxides that inhibit the reduction ability of Fe^0, but the formed passivation coating can combine with MoS_2 to assemble a heterojunction and induce further TC degradation. Moreover, 100% of TC removal is achieved via Fe@MS-2 after 30 min of visible-light irradiation (Fig. S3d, 20 $mg \cdot L^{-1}$ of TC solution). Even for a 50 $mg \cdot L^{-1}$ TC solution, the material can exhibit 86.96% of TC removal.

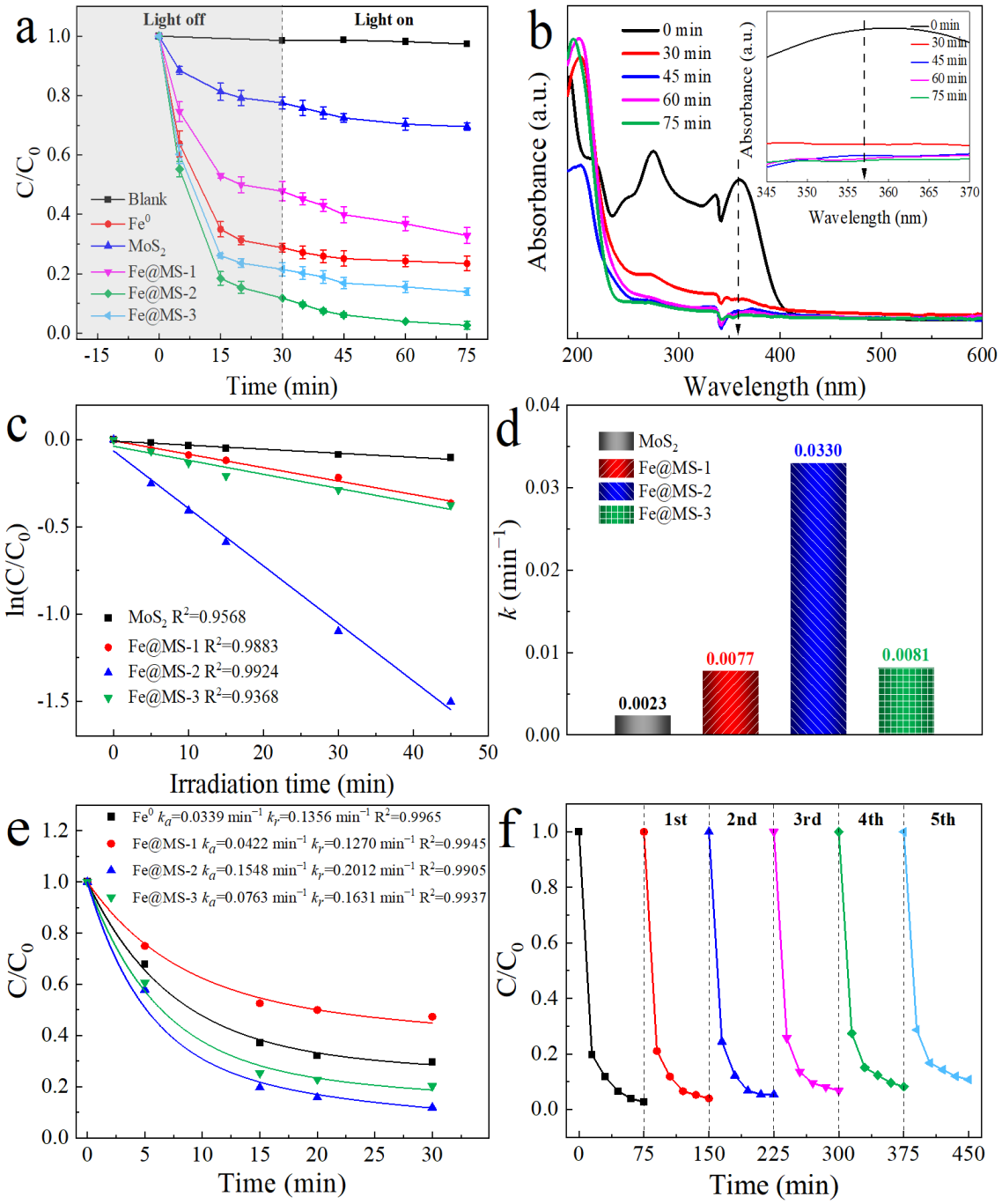

Fig. 4. (a) Comparation of photodegradation efficiency of nanomaterials for photodegradation of TC. (b) UV–vis absorption spectra related to TC photodegradation on Fe@MS-2. Results of (c)

pseudo-first-order kinetics, (d) related reaction rate constants, and (e) corrected pseudo-first-order kinetics of nanomaterials. (f) Results of the 5-cycle test with Fe@MS-2. (Experimental conditions: pH = 6.5; 10 mg of catalysts; 60 mL of 30 $mg \cdot L^{-1}$ TC solution)

Table 1 Comparison of photodegradation performance (TC) of catalysts in related literatures.

Catalyst	Dosage (mg)	C_0 ($mg \cdot L^{-1}$)	Volume (mL)	Time (min)	Removal (%)	Light source	Ref.
$MoS_2/CaTiO_3$	50	10	100	60	71.7	300 W xenon lamp	Jiang et al., 2020
$MoS_2@Fe_3O_4@Cu_2O$	10	20	100	90	68.61	300 W xenon lamp with UV filter	Li et al., 2021
$MoS_2/ZnSnO_3$	25	30	50	60	80.2	300 W xenon lamp ($\lambda > 420$ nm)	Guo et al., 2020
$CoS_2/MoS_2@$ Zeolite	10	200	50	120	96.71	300 W xenon lamp ($\lambda > 420$ nm)	Liu et al., 2020
$BiOI/MoS_2$	20	20	65	75	91.6	–	Guo et al., 2021
$MnFe_2O_4/MoS_2$	20	20	100	60	80.9	300 W xenon lamp	Wei et al., 2022
MoS_2/COF	10	20	20	60	85.9	300 W xenon lamp	Khaing et al., 2020
Bi_2O_3/MoS_2	50	30	50	100	97.0	250 W xenon lamp ($\lambda > 400$ nm)	Ma et al., 2019
$ZnS@MoS_2$	100	20	300	60	100	UV light	Zhang et al., 2020
$Fe^0@MoS_2$	10	30	60	45	97.37	300 W xenon lamp ($\lambda > 420$ nm)	This work

The degradation process and structural damage of TC are observed using the UV–vis absorption spectra of Fe@MS-2. The feature absorption peak intensity (Fig. 4b) of tetracycline at 357 nm shows a significant decrease and eventually almost disappear as the degradation experiment proceeds. It should be mentioned that the weakening of characteristic peak is accompanied by the change of absorption band around 200 nm, which indirectly explains the generation of TC-related intermediates (Wang et al., 2018).

Pseudo-first-order kinetics model is utilized for depicting the visible-light photodegradation kinetics of TC on Fe@MS-2. As shown in Fig. 4c, the goodness of fit of all materials is greater than

0.9, indicating that the photodegradation behavior of TC can be properly characterized by the pseudo-first-order kinetics. Correspondingly, the TC photodegradability of materials is quantified using reaction rate constant k (Fig. 4d). The order of k values of various materials is as follows: Fe@MS-2 > Fe@MS-3 > Fe@MS-1 > MoS_2, and the results show that Fe@MS-2 exhibits more excellent TC photodegradation ability compared to other materials. Moreover, the k value of Fe@MS-2 is 14.35 times higher than that of bare MoS_2, denoting the key role of Fe^0 doping on the efficient photodegradation of TC.

During the lightless reaction phase, the effects of nZVI-based composites on TC include adsorption and chemical reduction, which means the pseudo-first-order model is no longer applicable to this stage. Therefore, a modified pseudo-first-order kinetics model (equation (2) below) is applied to explain the existence of adsorption and reduction procedures, as proposed by our research group previously (Wang et al., 2018):

$$C_{eq} / C_{ini} = \alpha \times \exp(-k_a \times k_r \times t) + (1 - \alpha) \times \exp(-k_r \times t) \quad (2)$$

where C_{ini} and C_{eq} denote the original level of tetracycline and the level of tetracycline at reaction time t (min) respectively; α as well as $1 - \alpha$ represent the weight values of adsorption and reduction, separately; k_a and k_r denote the rate constants of adsorption and reduction, separately. The goodness of fit of all the fitted curves is higher than 0.99 (Fig. 4e), signifying the elimination of tetracycline by Fe@MS-2 during the dark reaction is in accordance with the modified pseudo-first-order kinetics. Furthermore, the k_a and k_r values of Fe@MS-2 are higher than that of other materials, proving its better adsorption and reduction capability relative to others, which are attributed to exposure of more available active sites.

A 5-cycle test of TC degradation is performed to verify the stability and recyclability of Fe@MS-2. The results in Fig. 4f demonstrate that the catalytic ability of the composite is not

significantly weakened after 5 cycles, showing its reliable stability. In the meantime, the composite can be readily detached from the pollutants with an imposed magnet due to its own magnetism (Fig. S4, 9.21 emu·g^{-1}; Fig. S5), which is convenient to be used again after being flushed and regenerated by UPW and a trace amount of KBH_4. Furthermore, there is no noticeable variation in the nanoflower framework of Fe@MS-2 before and after the photodegradation reaction, indicating the composite exhibits excellent structural stability (Fig. S6). These results reveal that Fe^0@MoS_2 shows a good application prospect in the area of environmental restoration.

3.3. Optical properties of nanomaterials

From the findings in XRD and XPS of Section 3.1, it is clear that a dense oxide layer (Fe_2O_3) is formed on the surface of Fe^0 after reacting in TC solution for 30 min. This passivation layer can prevent the contact between Fe^0 and TC and thus inhibits the reactivity of Fe^0 in the absence of a driving factor (light or heat source, etc.). From the viewpoint of photocatalysis, Fe_2O_3 is a composite which can accept a wide range of solar light (Wang et al., 2021; Zhao et al., 2021; Zhang et al., 2021). Inspired by this, this study proposes to use photocatalytic technology to activate the oxide layer into a semiconductor, and build a heterojunction with MoS_2 to achieve efficient photodegradation of TC. Therefore, the optical properties of related nanomaterials are tested to investigate their photodegradability and the feasibility of constructing heterojunctions. As illustrated in Fig. 5a, the photoluminescence (PL) strength of Fe_2O_3@MS-2 is significantly lower compared with that of bare MoS_2, implying a stronger separation of photo-generated charges in the composite relative to that in bare MoS_2. The smaller electronic impedance (Fig. 5b) and larger photocurrent response (Fig. 5c) of Fe_2O_3@MS-2 compared with pristine MoS_2 indicate that the segregation and migration rate of photo-excited carriers in the composite is notably higher than that in the single material. Combining the above results, it can be deduced that a built-in electric field is constructed

in the heterojunction of Fe_2O_3@MS-2, which effectively ensures the segregation and transport of photo-excited electron-hole pairs, thereby showing excellent light utilization ability (Liao et al., 2022). Moreover, the conductivity of MoS_2 is markedly boosted owing to the incorporation of the oxide layer of Fe^0.

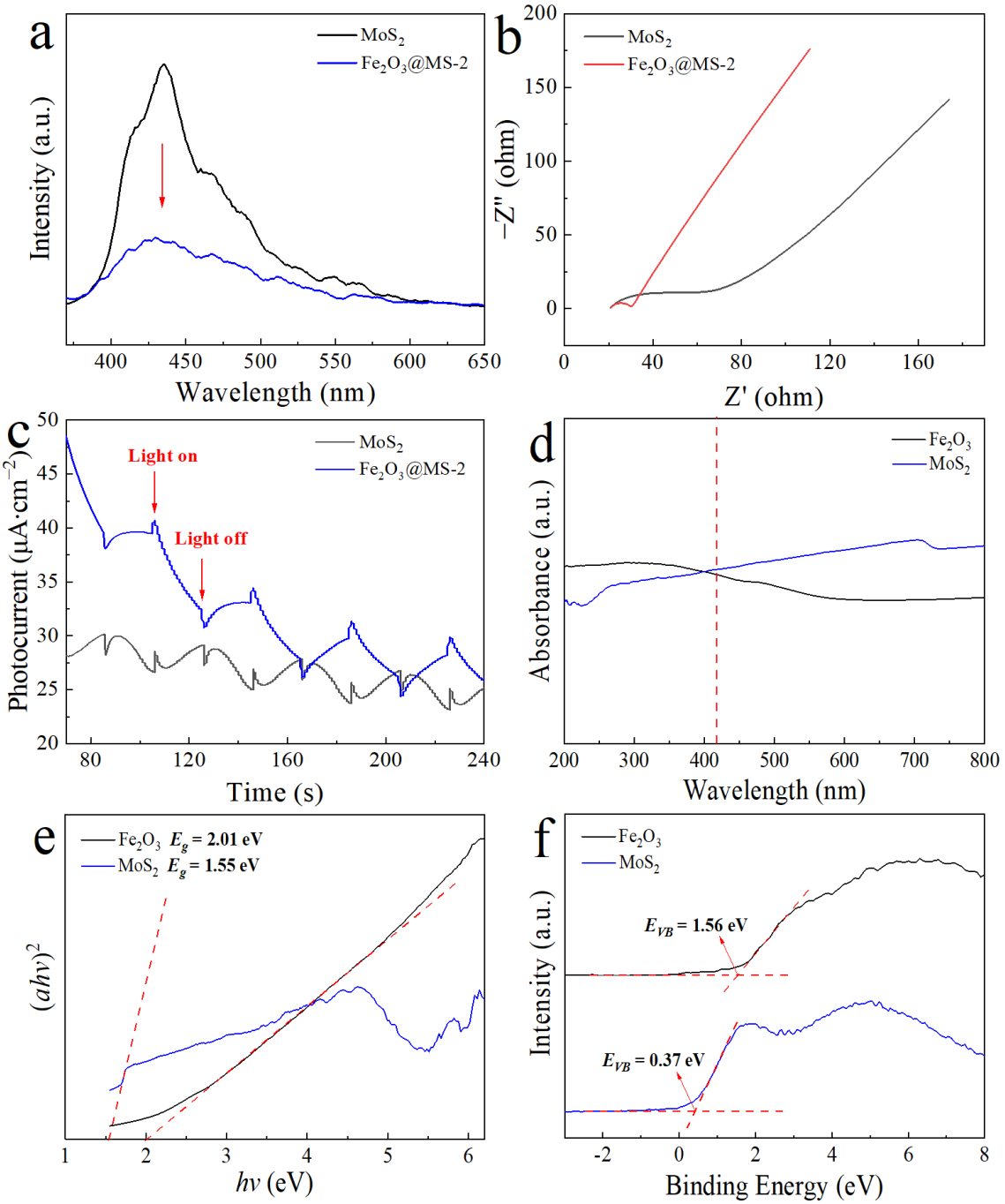

Fig. 5. (a) PL spectra, (b) electrochemical impedance spectroscopy (EIS) and (c) transient photocurrent responses for MoS_2 with Fe_2O_3@MS-2. (d) UV–vis DRS, (e) Tauc plots, (f) VB-XPS for Fe_2O_3 with MoS_2.

The ultraviolet–visible diffuse reflectance spectroscopy (UV–vis DRS) of Fe_2O_3 and MoS_2 are measured to determine their light absorption range. Interestingly, as shown in Fig. 5d, the light reception field of Fe_2O_3 and MoS_2 contains both ultraviolet and visible ranges, and both exhibit superior absorption capacity for visible-light. This result is favorable for the visible-light photocatalysis towards tetracycline on Fe@MS-2. The energy band structures of Fe_2O_3 and MoS_2 are analyzed by Tauc plots and VB-XPS. It can be derived from Fig. 5e that the band gap energies (E_g) of Fe_2O_3 and MoS_2 are 2.01 eV and 1.55 eV, respectively, and their narrow band gaps facilitate the absorption of visible-light and the transport of charges (Khaing et al., 2020). The valence band (VB) energies (E_{VB}) of both are 1.56 eV and 0.37 eV (Fig. 5f), respectively, thus, the conduction band (CB) energies (E_{CB}) of Fe_2O_3 and MoS_2 are calculated to be −0.45 eV and −1.18 eV individually, based on $E_g = E_{VB} - E_{CB}$ (Wang et al., 2022).

For grasping the critical reactive species of TC photodegradation over Fe@MS-2 to elucidate the photodegradation mechanism, free radical capturing tests and electron spin resonance (ESR) spectra are performed. In capturing tests, p-benzoquinone (p-BQ), dimethyl sulfoxide (DMSO), ammonium oxalate (AO) and methanol are employed as scavengers of $\bullet O_2^-$, e^-, h^+ and •OH, separately.

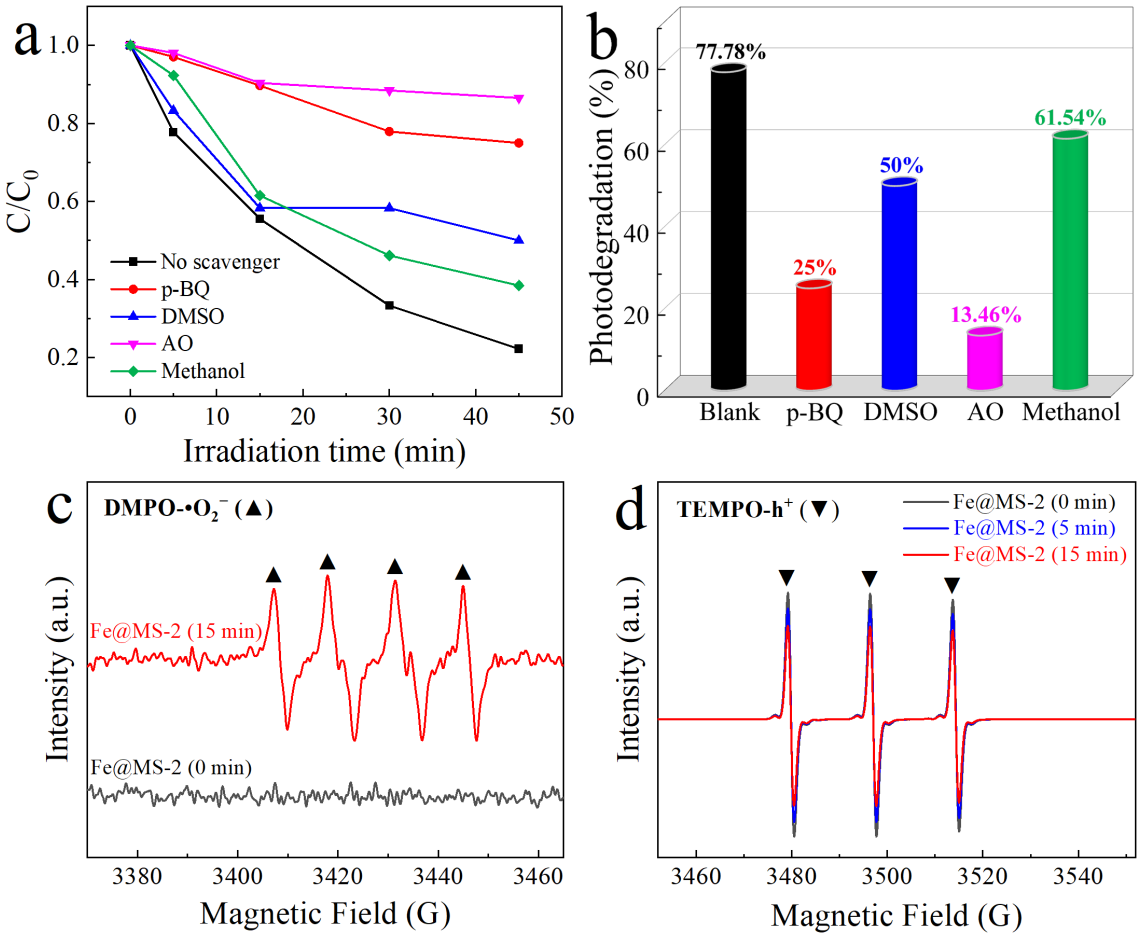

Fig. 6. (a) Results of free radical capturing tests and (b) the effect of different scavengers on photodegradation with Fe@MS-2. ESR spectra of (c) DMPO-•O_2^- and (d) TEMPO-h^+ of Fe@MS-2.

Combining the results in Fig. 6a and 6b, it is clear that the photodegradation efficiency of Fe@MS-2 to TC in the photoreaction stage is 77.78%, and the inhibitory ability of scavengers is in the following order: AO (13.46%) > p-BQ (25%) > DMSO (50%) > methanol (61.54%). Apparently, •O_2^- and h^+ are the key reactive species for the photo-elimination of TC on Fe@MS-2. In view of this, the role of superoxide radicals and holes is further analyzed using ESR spectra. As shown in Fig. 6c, no signal is detected on Fe@MS-2 in the absence of light. However, 4 distinct •O_2^- signature peaks with signal intensity of 1:1:1:1 are observed under visible-light radiation for 15 min. This phenomenon explains the formation and key role of •O_2^- during the photodegradation of tetracycline on Fe@MS-2. In ESR spectra of TEMPO-h^+ (Fig. 6d), the signal intensity associated

with photo-generated h^+ progressively fades with the prolongation of visible-light radiation time. The result indicates the efficient separation, transfer and strong oxidation of h^+ in Fe@MS-2 during visible-light irradiation, as confirmed in PL spectra, EIS and transient photocurrent responses. Therefore, it can be deduced that $\bullet O_2^-$ and photo-generated h^+ play key roles in the photodegradation of TC on Fe@MS-2.

3.4. Photodegradation mechanism and pathways

Profited from the findings of free radical capturing tests and ESR spectra in Section 3.3, and combining the energy band structures of Fe_2O_3 and MoS_2, a novel and efficient S-scheme heterojunction is proposed to be responsible for the efficient photodegradation of TC over Fe@MS-2 (Xu et al., 2020). In detail, after the heterojunction is excited with visible-light, the active photo-electrons on Fe_2O_3 and MoS_2 migrate from their VB to CB, resulting in photo-excited holes being left on their VB. Subsequently, electrons on the CB of MoS_2 preferentially react with dissolved oxygen to generate $\bullet O_2^-$ ($E(O_2/\bullet O_2^-)$ = −0.33 eV) due to the more negative redox potential of its CB (−1.18 eV) relative to that of CB (−0.45 eV) on Fe_2O_3 (Ma et al., 2019). Meanwhile, the oxidation ability of the holes of VB (1.56 eV) on Fe_2O_3 is obviously stronger than that of VB (0.37 eV) on MoS_2, and the redox potential of its VB is more negative than that of $\bullet OH/OH^-$ (1.99 eV) (Ma et al., 2019). Therefore, hydroxyl radicals cannot be generated on the VB of Fe_2O_3 and the TC adsorbed on it will be preferentially and directly degraded by its holes. Immediately afterwards, the e^- of CB on Fe_2O_3 are shifted to the VB of MoS_2 and bonded with the h^+ on it. Such an S-scheme heterojunction is undoubtedly favorable for the segregation and utilization of photo-excited electron-hole pairs, thereby ensuring the efficient photodegradation of TC.

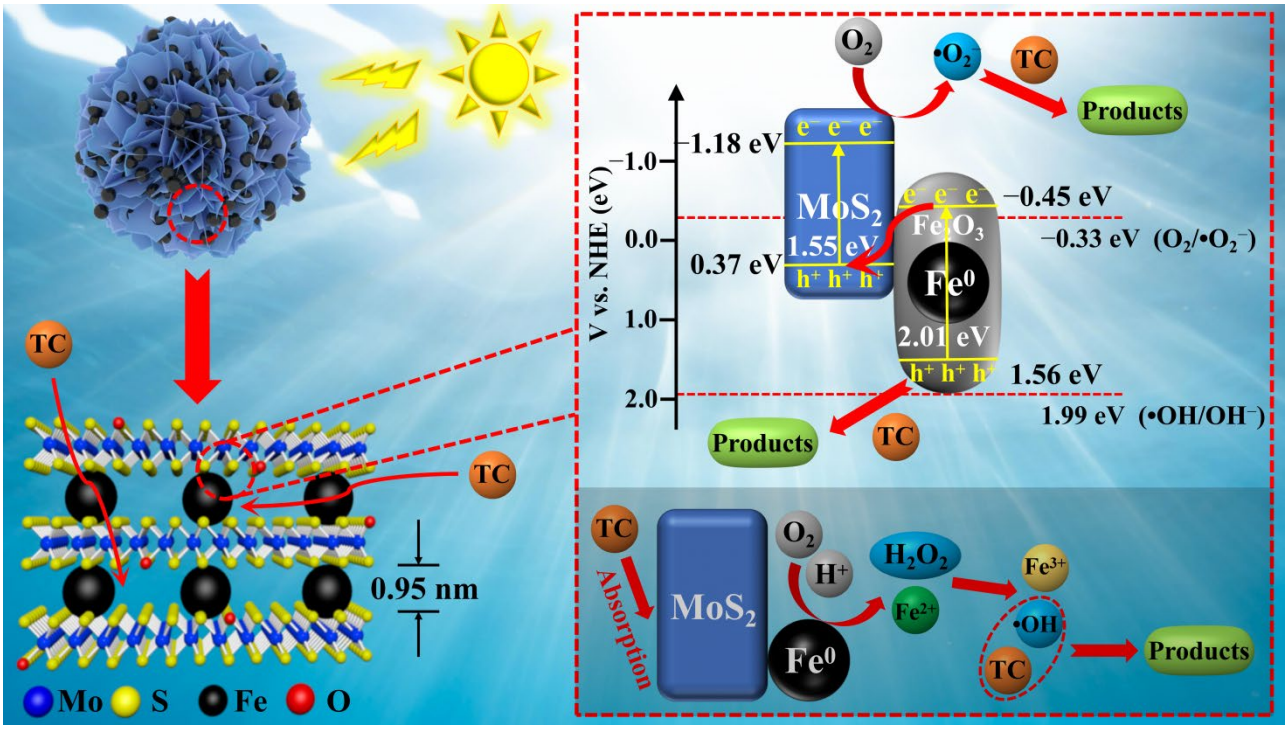

Fig. 7. Schematic diagram of the degradation mechanism of TC on Fe@MS-2.

The degradation mechanism of TC on Fe@MS-2 is thoroughly elucidated in consideration of the above conclusions (Fig. 7). Generally, the degradation of TC by Fe^0-based nanomaterials consists of 2 phases, adsorption and reduction in the dark reaction and photodegradation in the photoreaction (Wang et al., 2018). In the dark reaction, TC is first adsorbed onto the nanoflower-like Fe@MS-2, and Fe^0 interacts with dissolved oxygen and hydrogen ions in the TC solution for yielding ferrous ion and H_2O_2, followed immediately by a Fenton-like reaction to generate Fe^{3+} and hydroxyl radicals (Tian et al., 2021). Then, TC is degraded by hydroxyl radicals generated by the Fenton-like process to produce intermediates, even CO_2 and H_2O. The detailed degradation process is shown in the following Eqs. (3)–(5):

$$TC + Fe@MS\text{-}2 \rightarrow TC\text{-}Fe@MS\text{-}2 \quad (3)$$

$$Fe^0 + O_2 + 2H^+ \rightarrow Fe^{2+} + H_2O_2 \rightarrow Fe^{3+} + \bullet OH + OH^- \quad (4)$$

$$TC\text{-}Fe@MS\text{-}2 + \bullet OH \rightarrow \text{intermediates} \rightarrow CO_2 + H_2O \quad (5)$$

In the photoreaction, the tight oxide coating (Fe_2O_3) on the outside of Fe^0 produced during dark reaction and MoS_2 are constructed as an S-scheme heterojunction. e^- on Fe_2O_3 and MoS_2 are diverted from their VB towards CB behind visible-light irradiation, along with h^+ being left on their VB. Afterwards, the e^- of CB on MoS_2 react with dissolved oxygen to generate $\bullet O_2^-$ due to its CB (−1.18 eV) is further minus than −0.33 eV of $E(O_2/\bullet O_2^-)$. Meanwhile, the potent oxidizing h^+ of VB on Fe_2O_3 directly react with TC to generate degradation products since its VB (1.56 eV) is less anodic compared with 1.99 eV of $E(\bullet OH/OH^-)$. And the h^+ of VB on MoS_2 are combined with the e^- of CB on Fe_2O_3. Furthermore, Fe^{3+} produced during dark reaction can be reduced by e^- to form Fe^{2+} (Tian et al., 2021). An experiment of Fe^{2+} leaching also validates such a cycle of iron species (Fig. S7). Cycling among ferrous with ferric ion ensures favorable photocatalytic stability of Fe@MS-2. Eventually, TC is degraded to CO_2 and H_2O attributed to the action of $\bullet O_2^-$ and h^+. The specific photocatalytic mechanism is as follows (Eqs. (6)–(12)):

$$Fe_2O_3 + h\nu \rightarrow h^+ + e^- \quad (6)$$

$$MoS_2 + h\nu \rightarrow h^+ + e^- \quad (7)$$

$$e^-\text{-CB}\,(MoS_2) + O_2 \rightarrow \bullet O_2^- \quad (8)$$

$$TC + h^+\text{-VB}\,(Fe_2O_3) \rightarrow \text{intermediates} \rightarrow CO_2 + H_2O \quad (9)$$

$$e^-\text{-CB}\,(Fe_2O_3) \rightarrow h^+\text{-VB}\,(MoS_2) \quad (10)$$

$$Fe^{3+} + e^- \rightarrow Fe^{2+} \quad (11)$$

$$TC + \bullet O_2^- \rightarrow \text{intermediates} \rightarrow CO_2 + H_2O \quad (12)$$

To distinguish the intermediates produced during photodegradation of TC and thus propose corresponding reaction pathways, liquid chromatography mass spectrometry (LC-MS) technique is employed to identify relevant substances by their mass-to-charge ratios (m/z). Based on the findings

of LC-MS displayed in Fig. S8, potential routes for the photodegradation of TC on Fe@MS-2 are presented.

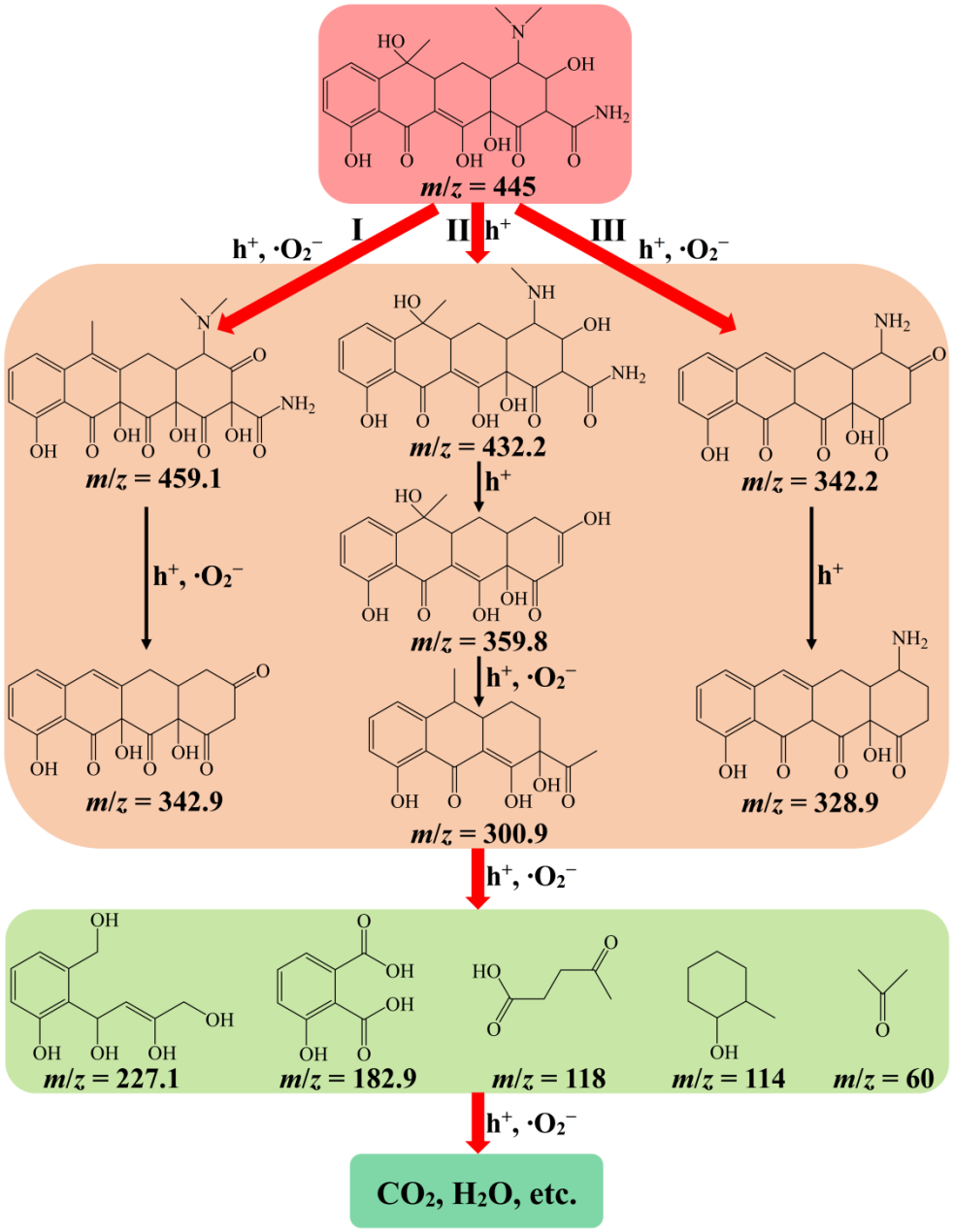

Fig. 8. potential routes of TC photodegradation on Fe@MS-2.

As shown in Fig. 8, 3 possible pathways are involved in the photodegradation of TC on Fe@MS-2 (Cao et al., 2016; Kumar et al., 2022; Li et al., 2021; Li et al., 2022; Ren et al., 2019; Shi et al., 2020). In route I, tetracycline (m/z = 445) is reacted as m/z = 459.1 via processes such as carbonylation and demethylation, followed by the formation of m/z = 342.9 through the steps of demethylation, deamination, deamidation and dehydroxylation. For route II, TC is degraded to m/z

= 432.2 via a demethylation step, and then degraded to *m*/*z* = 359.8 due to the effect of N-demethylation and deamidation. Afterwards, dehydroxylation and ring-opening reaction result in the creation of *m*/*z* = 300.9. In route III, tetracycline is decomposed into *m*/*z* = 342.2 attributed to demethylation, dehydroxylation, carbonylation and deamidation. Subsequently, the generation of *m*/*z* = 328.9 derives from a decarbonylation step. After that, these substances are further decomposed into *m*/*z* = 227.1, 182.9, 118, 114 and 60. Eventually these intermediates will be degraded into CO_2 and H_2O. The above degradation steps are ascribed to the attack of superoxide radicals and holes, which again proves their critical role in the photodegradation of TC on Fe@MS-2.

4. Conclusions

Novel Fe^0@MoS_2 nanoflower S-scheme heterojunction catalyst exhibiting superior photocatalytic ability for tetracycline was prepared. The findings showed that the photodegradation efficiency of Fe@MS-2 for TC was 97.37% under 45 min of visible-light illumination, which was 3.20 and 1.27 folds higher than that of pristine MoS_2 and Fe^0, respectively. SEM, XRD and TEM findings proved MoS_2 nanoflowers were composed of plenty of oxygen-incorporated ultrathin nanosheets, and their widened interlayer spacing was induced by Fe^0. The fluffy nanoflower-like structure and widened interlayer spacing of MoS_2 promoted the high confinement and dispersion of Fe^0, which achieved a rise in the amount of available reactive centers of Fe^0, ensuring its potent adsorption and reducing properties. Conversely, the results of XRD and XPS indicated the creation of a dense passivation coating (Fe_2O_3) on the surface of Fe^0, and the oxide layer improved the conductivity of MoS_2, as evidenced by the transient photocurrent response and EIS, which cooperated with MoS_2 to construct this S-scheme heterojunction. Obviously, the synergistic effect between Fe^0 and MoS_2 was favorable for the efficient photodegradation of TC on Fe@MS-2.

Furthermore, the excellent stability, recyclability, kinetics of Fe@MS-2 as well as the boosted segregation and migration performance of photo-excited carriers of Fe_2O_3@MS-2 were confirmed. Moreover, potential pathways for TC photodegradation ascribed to the critical action of $\bullet O_2^-$ and h^+ were also proposed. This work innovatively presented a idea of using photocatalytic technology to activate the oxide coating of Fe^0 into a semiconductor and further establish a novel and efficient S-scheme heterojunction with MoS_2 for environmental restoration.

Acknowledgments

This work was supported by the National Natural Science Foundation of China (NSFC, Grant No. 51968031), State Scholarship Fund of China Scholarship Council (CSC) via which Xiangyu Wang was a visiting Professor at the University of Birmingham, the Engineering and Physical Sciences Research Council Impact Acceleration Accounts Developing Leaders (Grant No. 1001634), and EU H2020 projects NanoSolveIT (Grant Agreement 814572), RiskGone (Grant Agreement 814425), NanoCommons (Grant Agreement 731032) and CompSafeNano (Grant Agreement 101008099).

References

Ahmaruzzaman, Md., Gadore, V., 2021. MoS_2 based nanocomposites: an excellent material for energy and environmental applications. J. Environ. Chem. Eng. 9, 105836.

Ai, K., Ruan, C., Shen, M., Lu, L., 2016. MoS_2 nanosheets with widened interlayer spacing for high-efficiency removal of mercury in aquatic systems. Adv. Funct. Mater. 26, 5542–5549.

Bai, J., Zhao, B., Zhou, J., Si, J., Fang, Z., Li, K., Ma, H., Dai, J., Zhu, X., Sun, Y., 2019. Glucose-induced synthesis of 1T-MoS_2/C hybrid for high-rate lithium-ion batteries. Small 15, 1805420.

Cao, M., Wang, P., Ao, Y., Wang, C., Hou, J., Qian, J., 2016. Visible light activated photocatalytic

degradation of tetracycline by a magnetically separable composite photocatalyst: graphene oxide/magnetite/cerium-doped titania. J. Colloid Interf. Sci. 467, 129–139.

Cao, Z., Li, H., Lowry, G.V., Shi, X., Pan, X., Xu, X., Henkelman, G., Xu, J., 2021. Unveiling the role of sulfur in rapid defluorination of florfenicol by sulfidized nanoscale zero-valent iron in water under ambient conditions. Environ. Sci. Technol. 55, 2628–2638.

Chen, D., Bai, Q., Ma, T., Jing, X., Tian, Y., Zhao, R., Zhu, G., 2022. Stable metal-organic framework fixing within zeolite beads for effectively static and continuous flow degradation of tetracycline by peroxymonosulfate activation. Chem. Eng. J. 435, 134916.

Chen, X., Liu, L., Huang, F., 2015. Black titanium dioxide (TiO_2) nanomaterials. Chem. Soc. Rev. 44, 1861–1885.

Chen, Y., Yin, H., Li, F., Zhou, J., Wang, L., Wang, J., Ai, S., 2020. Polydopamine-sensitized WS_2/black-TiO_2 heterojunction for histone acetyltransferase detection with enhanced visible-light-driven photoelectrochemical activity. Chem. Eng. J. 393, 124707.

Fang, Z., Qiu, X., Chen, J., Qiu, X., 2010. Degradation of metronidazole by nanoscale zero-valent metal prepared from steel pickling waste liquor. Appl. Catal. B: Environ. 100, 221–228.

Guo, F., Huang, X., Chen, Z., Ren, H., Li, M., Chen, L., 2020. MoS_2 nanosheets anchored on porous $ZnSnO_3$ cubes as an efficient visible-light-driven composite photocatalyst for the degradation of tetracycline and mechanism insight. J. Hazard. Mater. 390, 122158.

Guo, S., Luo, H., Li, Y., Chen, J., Mou, B., Shi, X., Sun, G., 2021. Structure-controlled three-dimensional BiOI/MoS_2 microspheres for boosting visible-light photocatalytic degradation of tetracycline. J. Alloy. Compd. 852, 157026.

Hou, J., Wang, C., Mao, D., Luo, Y., 2016. The occurrence and fate of tetracyclines in two pharmaceutical wastewater treatment plants of Northern China. Environ. Sci. Pollut. Res. 23,

1722–1731.

Hu, L., Wang, R., Wang, M., Wang, C., Xu, Y., Wang, Y., Gao, P., Liu, C., Song, Y., Ding, N., Liu, Y., Chen, J., 2022. The inactivation effects and mechanisms of *Karenia mikimotoi* by non-metallic elements modified TiO_2 (SNP-TiO_2) under visible light. Sci. Total Environ. 820, 153346.

Hu, L., Chen, J., Wei, Y., Wang, M., Xu, Y., Wang, C., Gao, P., Liu, Y., Liu, C., Song, Y., Ding, N., Liu, X., Wang, R., 2023. Photocatalytic degradation effect and mechanism of *Karenia mikimotoi* by non-noble metal modified TiO_2 loading onto copper metal organic framework (SNP-TiO_2@Cu-MOF) under visible light. J. Hazard. Mater. 442, 130059.

Hu, Y., Li, X., 2018. Influence of a thin aluminum hydroxide coating layer on the suspension stability and reductive reactivity of nanoscale zero-valent iron. Appl. Catal. B: Environ. 226, 554–564.

Jiang, E., Song, N., Che, G., Liu, C., Dong, H., Yang, L., 2020. Construction of a Z-scheme MoS_2/$CaTiO_3$ heterostructure by the morphology-controlled strategy towards enhancing photocatalytic activity. Chem. Eng. J. 399, 125721.

Khaing, K.K., Yin, D., Ouyang, Y., Xiao, S., Liu, B., Deng, L., Li, L., Guo, X., Wang, J., Liu, J., Zhang, Y., 2020. Fabrication of 2D–2D heterojunction catalyst with covalent organic framework (COF) and MoS_2 for highly efficient photocatalytic degradation of organic pollutants. Inorg. Chem. 59, 6942–6952.

Kumar, A., Thakur, P.R., Sharma, G., Vo, D.V.N., Naushad, M., Tatarchuk, T., García-Peñas, A., Du, B., Stadler, F.J., 2022. Accelerated charge transfer in well-designed S-scheme Fe@TiO_2/Boron carbon nitride heterostructures for high performance tetracycline removal and selective photo-reduction of CO_2 greenhouse gas into CH_4 fuel. Chemosphere 287, 132301.

Li, H., Liu, Y., Liu, Y., Wang, L., Tang, R., Deng, P., Xu, Z., Haynes, B., Sun, C., Huan, J., 2021. Efficient visible light driven ammonia synthesis on sandwich structured $C_3N_4/MoS_2/Mn_3O_4$ catalyst. Appl. Catal. B: Environ. 281, 119476.

Li, M., Luo, R., Wang, C., Zhang, M., Zhang, W., Klu, P.K., Yan, Y., Qi, J., Sun, X., Wang, L., Li, J., 2019. Iron-tannic modified cotton derived Fe^0/graphitized carbon with enhanced catalytic activity for bisphenol A degradation. Chem. Eng. J. 372, 774–784.

Li, M., Shang, H., Li, H., Hong, Y., Ling, C., Wei, K., Zhou, B., Mao, C., Ai, Z., Zhang, L., 2021. Kirkendall effects boosts phosphorylated nZVI for efficient heavy metal wastewater treatment. Angew. Chem. Int. Ed. 133, 17252–17259.

Li, W., Zhou, G., Zhu, X., Song, M., Wang, P., Ma, C., Liu, X., Han, S., Huang, Y., Lu, Z., 2021. Magnetic assembly synthesis of high-efficiency recyclable flower-like $MoS_2@Fe_3O_4@Cu_2O$ like-Z-scheme heterojunction towards efficient photodegradation of tetracycline. Appl. Surf. Sci. 555, 149730.

Li, X., Qiu, Y., Zhu, Z., Zhang, H., Yin, D., 2022. Novel recyclable Z-scheme g-C_3N_4/carbon nanotubes/$Bi_{25}FeO_{40}$ heterostructure with enhanced visible-light photocatalytic performance towards tetracycline degradation. Chem. Eng. J. 429, 132130.

Li, Z., Fan, R., Hu, Z., Li, W., Zhou, H., Kang, S., Zhang, Y., Zhang, H., Wang, G., 2020. Ethanol introduced synthesis of ultrastable 1T-MoS_2 for removal of Cr(VI). J. Hazard. Mater. 394, 122525.

Li, Z., Ma, H., Zang, L., Li, D., Guo, S., Shi, L., 2021. Construction of nano-flower MIL-125(Mo)-In_2Se_3 Z-scheme heterojunctions by one-step solvothermal method for removal of tetracycline from wastewater in the synergy of adsorption and photocatalysis way. Separ. Purif. Technol. 276, 119355.

Liao, B., Liao, X., Xie, H., Qin, Y., Zhu, Y., Yu, Y., Hou, S., Zhang, Y., Fan, X., 2022. Built in electric field boosted photocatalytic performance in a ferroelectric layered material $SrBi_2Ta_2O_9$ with oriented facets: charge separation and mechanism insights. J. Mater. Sci. Technol. 123, 222–233.

Ling, L., Zhang, W., 2015. Enrichment and encapsulation of uranium with iron nanoparticle. J. Am. Chem. Soc. 137, 2788–2791.

Liu, J., Lin, H., Dong, Y., He, Y., Liu, C., 2022a. MoS_2 nanosheets loaded on collapsed structure zeolite as a hydrophilic and efficient photocatalyst for tetracycline degradation and synergistic mechanism. Chemosphere 287, 132211.

Liu, J., Lin, H., He, Y., Dong, Y., Menzembere, E.R.G.Y., 2020. Novel CoS_2/MoS_2@Zeolite with excellent adsorption and photocatalytic performance for tetracycline removal in simulated wastewater. J. Clean. Prod. 260, 121047.

Liu, K., Chen, J., Sun, F., Liu, Y., Tang, M., Yang, Y., 2022b. Historical development and prospect of intimately coupling photocatalysis and biological technology for pollutant treatment in sewage: A review. Sci. Total Environ. 835, 155482.

Liu, K., Yang, Y., Sun, F., Liu, Y., Tang, M., Chen, J., 2022c. Rapid degradation of Congo red wastewater by *Rhodopseudomonas palustris* intimately coupled carbon nanotube - Silver modified titanium dioxide photocatalytic composite with sodium alginate. Chemosphere 299, 134417.

Lu, X., Wang, Y., Zhang, X., Xu, G., Wang, D., Lv, J., Zheng, Z., Wu, Y., 2018. NiS and MoS_2 nanosheet co-modified graphitic C_3N_4 ternary heterostructure for high efficient visible light photodegradation of antibiotic. J. Hazard. Mater. 341, 10–19.

Ma, Z., Hu, L., Li, X., Deng, L., Fan, G., He, Y., 2019. A novel nano-sized MoS_2 decorated Bi_2O_3

heterojunction with enhanced photocatalytic performance for methylene blue and tetracycline degradation. Ceram. Int. 45, 15824–15833.

Qiao, J., Song, Y., Sun, Y., Guan, X., 2018. Effect of solution chemistry on the reactivity and electron selectivity of zerovalent iron toward Se(VI) removal. Chem. Eng. J. 353, 246–253.

Ren, L., Zhou, W., Sun, B., Li, H., Qiao, P., Xu, Y., Wu, J., Lin, K., Fu, H., 2019. Defects-engineering of magnetic γ-Fe_2O_3 ultrathin nanosheets/mesoporous black TiO_2 hollow sphere heterojunctions for efficient charge separation and the solar-driven photocatalytic mechanism of tetracycline degradation. Appl. Catal. B: Environ. 240, 319–328.

Shao, Y., Gao, Y., Yue, Q., Kong, W., Gao, B., Wang, W., Jiang, W., 2020. Degradation of chlortetracycline with simultaneous removal of copper (II) from aqueous solution using wheat straw-supported nanoscale zero-valent iron. Chem. Eng. J. 379, 122384.

Shi, Q., Zhang, Y., Sun, D., Zhang, S., Tang, T., Zhang, X., Cao, S., 2020. Bi_2O_3-sensitized TiO_2 hollow photocatalyst drives the efficient removal of tetracyclines under visible light. Inorg. Chem. 59, 18131–18140.

Sun, H., Wu, T., Zhang, Y., Ng, D.H.L., Wang, G., 2018. Structure-enhanced removal of Cr(VI) in aqueous solutions using MoS_2 ultrathin nanosheets. New J. Chem. 42, 9006–9015.

Tian, Y., Zhou, M., Pan, Y., Du, X., Wang, Q., 2021. MoS_2 as highly efficient co-catalyst enhancing the performance of Fe^0 based electro-Fenton process in degradation of sulfamethazine: approach and mechanism. Chem. Eng. J. 403, 126361.

Wang, H.Y., Hu, R., Wang, N., Hu, G.L., Wang, K., Xie, W.H., Cao, R., 2021. Boosting photoanodic activity for water splitting in carbon dots aqueous solution without any traditional supporting electrolyte. Appl. Catal. B: Environ. 296, 120378.

Wang, J., Cao, C.S., Wang, J., Zhang, Y., Zhu, L., 2022. Insights into highly efficient

photodegradation of poly/perfluoroalkyl substances by In-MOF/BiOF heterojunctions: built-in electric field and strong surface adsorption. Appl. Catal. B: Environ. 304, 121013.

Wang, Q., Huang, J., Sun, H., Ng, Y.H., Zhang, K.Q., Lai, Y., 2018. MoS_2 quantum dots@TiO_2 nanotube arrays: an extended-spectrum-driven photocatalyst for solar hydrogen evolution. ChemSusChem 11, 1708–1721.

Wang, X., Wang, A., Lu, M., Ma, J., 2018. Synthesis of magnetically recoverable Fe^0/graphene-TiO_2 nanowires composite for both reduction and photocatalytic oxidation of metronidazole. Chem. Eng. J. 337, 372–384.

Wei, X., Yi, H., Lai, C., Huo, X., Ma, D., Du, C., 2022. Synergistic effect of flower-like $MnFe_2O_4$/MoS_2 on photo-Fenton oxidation remediation of tetracycline polluted water. J. Colloid Interf. Sci. 608, 942–953.

Weng, X., Cai, W., Owens, G., Chen, Z., 2021. Magnetic iron nanoparticles calcined from biosynthesis for fluoroquinolone antibiotic removal from wastewater. J. Clean. Prod. 319, 128734.

Wu, M., Li, L., Liu, N., Wang, D., Xue, Y., Tang, L., 2018. Molybdenum disulfide (MoS_2) as a co-catalyst for photocatalytic degradation of organic contaminants: a review. Process Saf. Environ. 118, 40–58.

Xie, J., Zhang, J., Li, S., Grote, F., Zhang, X., Zhang, H., Wang, R., Lei, Y., Pan, B., Xie, Y., 2013. Controllable disorder engineering in oxygen-incorporated MoS_2 ultrathin nanosheets for efficient hydrogen evolution. J. Am. Chem. Soc. 135, 17881–17888.

Xu, J., Wang, Y., Weng, C., Bai, W., Jiao, Y., Kaegi, R., Lowry, G.V., 2019. Reactivity, selectivity, and long-term performance of sulfidized nanoscale zerovalent iron with different properties. Environ. Sci. Technol. 53, 5936–5945.

Xu, Q., Zhang, L., Cheng, B., Fan, J., Yu, J., 2020. S-scheme heterojunction photocatalyst. Chem 6, 1–17.

Zhang, K., Meng, W., Wang, S., Mi, H., Sun, L., Tao, K., 2020. One-step synthesis of ZnS@MoS_2 core-shell nanostructure for high efficiency photocatalytic degradation of tetracycline. New J. Chem. 44, 472–477.

Zhang, X., Lai, Z., Tan, C., Zhang, H., 2016. Solution-processed two-dimensional MoS_2 nanosheets: preparation, hybridization, and applications. Angew. Chem. Int. Ed. 55, 2–25.

Zhang, Y., Huang, Y., Zhu, S.S., Liu, Y.Y., Zhang, X., Wang, J.J., Braun, A., 2021. Covalent S–O bonding enables enhanced photoelectrochemical performance of Cu_2S/Fe_2O_3 heterojunction for water splitting. Small 17, 2100320.

Zhang, Z., Liu, C., Dong, Z., Dai, Y., Xiong, G., Liu, Y., Wang, Y., Wang, Y., Liu, Y., 2020. Synthesis of flower-like MoS_2/g-C_3N_4 nanosheet heterojunctions with enhanced photocatalytic reduction activity of uranium(VI). Appl. Surf. Sci. 520, 146352.

Zhao, M., Ma, X., Yan, S., Xiao, H., Li, Y., Hu, T., Zheng, Z., Jia, J., Wu, H., 2020. Solvothermal synthesis of oxygen-incorporated MoS_{2-x} nanosheets with abundant under coordinated Mo for efficient hydrogen evolution. Int. J. Hydrogen Energy 45, 19133–19143.

Zhao, Y., Deng, C., Tang, D., Ding, L., Zhang, Y., Sheng, H., Ji, H., Song, W., Ma, W., Chen, C., Zhao, J., 2021. α-Fe_2O_3 as a versatile and efficient oxygen atom transfer catalyst in combination with H_2O as the oxygen source. Nat. Catal. 4, 684–691.

Zheng, L., Han, S., Liu, H., Yu, P., Fang, X., 2016. Hierarchical MoS_2 nanosheet@TiO_2 nanotube array composites with enhanced photocatalytic and photocurrent Performances. Small 12, 1527–1536.

Zhou, J., Li, X., Yuan, J., Wang, Z., 2022. Efficient degradation and toxicity reduction of

tetracycline by recyclable ferroferric oxide doped powdered activated charcoal via peroxymonosulfate (PMS) activation. Chem. Eng. J. 441, 136061.

Zhou, L., Li, Z., Yi, Y., Tsang, E.P., Fang, Z., 2022. Increasing the electron selectivity of nanoscale zero-valent iron in environmental remediation: a review. J. Hazard. Mater. 421, 126709.

Zhou, Y., Gao, Y., Jiang, J., Shen, Y.M., Pang, S.Y., Wang, Z., Duan, J., Guo, Q., Guan, C., Ma, J., 2020. Transformation of tetracycline antibiotics during water treatment with unactivated peroxymonosulfate. Chem. Eng. J. 379, 12237.

Zhu, Q., Sun, Y., Na, F., Wei, J., Xu, S., Li, Y., Guo, F., 2019. Fabrication of CdS/titanium-oxo-cluster nanocomposites based on a Ti_{32} framework with enhanced photocatalytic activity for tetracycline hydrochloride degradation under visible light. Appl. Catal. B: Environ. 254, 541–550.